Extreme curvature of shallow magma pathways controlled by competing stresses

Timothy Davis[1], Marco Bagnardi[2,3], Paul Lundgren[3], Eleonora Rivalta[1,4]

[1]GFZ (GeoForschungsZentrum), Physics of Earthquakes and Volcanoes, Helmholtzstraße 6/7, Building H 7, 14467 Potsdam. {davis,rivalta}@gfz-potsdam.de

[2]Now at Cryospheric Sciences Laboratory, NASA Goddard Space Flight Center, 8800 Greenbelt Road, Greenbelt, MD, United States. marco.bagnardi@nasa.gov

[3]Jet Propulsion Laboratory, California Institute of Technology, 4800 Oak Grove Drive, Pasadena, CA, United States. paul.r.lundgren@jpl.nasa.gov

[4]Department of Physics and Astronomy, Alma Mater Studiorum University of Bologna, V.le Berti Pichat 6. eleonora.rivalta@unibo.it

Summary paragraph

To feed off-summit eruptions at volcanoes, magma moves by creating and passing through cracks that can propagate many kilometres downslope. Typically, these cracks are vertical (dykes). Here we show the propagation of a flat-lying magma-filled crack (sill) at Sierra Negra volcano, Galápagos Islands, using space-borne radar interferometric data spanning the 2018 eruption. This sill propagated along a 15-km-long curved trajectory, which is hard to explain with current understanding and models. We develop both a simple analytical analysis and a three dimensional (3D) numerical crack propagation model, which incorporates the effects of magma buoyancy, realistic topography and tectonic forces that may control the sill's propagation. We show that sill trajectories can only be understood and predicted if accounting for the interaction of all these factors, and explain the observed trajectory at Sierra Negra as the result of competing stresses being close to one another throughout the

Corresponding author: Timothy Davis, `davis@gfz-potsdam.de`

propagation of the sill. Under certain conditions, these events may be inherently unstable but remain predictable by combining high resolution observations with sophisticated theoretical understanding.

1 Introduction

Sierra Negra is an intra-plate basaltic shield volcano with a maximum elevation of 1140 m above sea level (a.s.l.), a shallow (110 m) and structurally complex 7 x 10 km elliptical caldera, and is the most voluminous of the five coalescing volcanoes that form Isabela Island in the western Galápagos Archipelago, Ecuador[1].

Thirteen effusive eruptions have occurred at Sierra Negra since 1813. The three most recent eruptions all occurred in the northern flank of the volcano and produced 0.90 km^3 in 1979, 0.15 km^3 in 2005, and 0.19 km^3 in 2018[2]. While the 1979 and 2005 eruptions were fed by vents high on the northern flank and with eruptive fissures aligned parallel to the caldera rim, the vents of the 2018 eruption were scattered with no preferred orientation up to 9.5 km from the caldera rim, at a minimum elevation of 90 m a.s.l. Vents at such low elevation do not seem to be common in the recent history of the volcano. On the other hand, some of the higher-elevation eruptive vents of the 2018 eruption reactivated existing fissures. The 2018 eruption interrupted a thirteen-year semi-continuous period of uplift that raised the floor of the summit caldera by up to 5.2 m since the 2005 eruption as measured by GPS (Extended Data Fig. 1), presumed to be re-pressurization of a ∼2 km deep magma reservoir. On the 26 June 2018 at 19h40 the appearance of volcanic tremor marked the beginning of the eruption. Throughout the eruption, seismicity was mainly located along the caldera fault system with fewer events in the northwestern upper flank. Caldera deflation rapidly started with the onset of eruptive activity and by the time the eruption ended on August 25th 2018, GPS stations measured a cumulative intra-caldera subsidence of up to ∼8.5 m (Extended Data Fig. 1).

Short-lived ($<$ 24 hrs) effusive eruptions from multiple fissures (Fissure 1 - 5, Fig. 1) on 26-27 June were followed by a long-lasting effusive eruption from the most distal fissure (Fissure 6) between July 1st and August 25th. Geodetic monitoring by continuous GPS at Sierra Negra is limited to the summit caldera, such that the feeder-induced surface displacements were only measured by interferometric synthetic aperture radar (InSAR). The first co-eruptive synthetic aperture radar (SAR) image was acquired on 29 June at 17:50 UTC by the Japan Aerospace Exploration Agency's ALOS-2 satellite, approximately 70 hours after the onset of the seismic swarm, Fig. 1. Further SAR images were acquired on 30 June and 1 July by the European Space Agency's Sentinel-1 satellite constellation, right before the opening of Fissure 6, Extended Data Fig. 2a and b. Additional SAR images were captured during the eruption of Fissure 6; Extended Data Fig. 3a and b.

Surface deformation patterns before and after Fissure 6 erupted show a surprising trajectory for the propagating feeder. The deformation patterns point at a flat-lying magma body (sill, see Methods) turning 90 degrees within its horizontal plane of propagation. Even though turning and twisting of dykes has been observed frequently[3–5], such a 90 degrees turn has never been observed before.

2 Parameters and numerical result

In order to understand why the sill turned as observed, before proceeding with a 3D simulation, we reduce the physics of this problem to its component parts and evaluate how these affect the sill's direction of propagation. Previous studies have found that dyke trajectories are dependent on the ratio of tectonic to topographic loading stresses[3,6,7]. Here we propose that contrasting magma and rock weight gradients (buoyancy) must also be considered as one of the dominant forces.

Propagation directions of dykes have typically been predicted by maximizing the strain energy release rate, $\mathcal{G}$[3,8], on test elongations at the leading tip, thereby finding the path of least resistance. Such a method is unwieldy for true 3D propagation, as it would involve computing a large number of potential tip-line growth patterns. Here we use a theoretically equivalent, but more flexible, approach based on the maximum stress intensity, K. In our analytical approach, we reduce the sill geometry to that of a penny-shaped crack subject to stress gradients (Supplementary Information), with an opening that is compatible with the surface displacements observed along the short-axis of the sill (see Methods). At selected points along the sill's path, we calculate K, around the tip-line[9], and assume the greatest tip-line advance occurs in the direction where K is largest (Paris fatigue law[10]). In our numerical simulations, we discretise the sill into triangular elements[10,11] and update the tip-line at each step using the local value of K as compared to the critical rock strength, K_c.

In our analytical approach, we employ stress intensity equations in a full-space. We then go on to numerically test how the free-surface and the real topography would affect these results. In the numerical simulations, we compute stresses under an arbitrary topography in 3D with an external elastic stress field. As in previous 3D studies we neglect viscous effects of the contained fluid and chamber pressure.

We constrain the parameters in both models using inversions of co-eruptive InSAR data along the propagation path (Fig. 1, see Methods): depth d=950 m, radius c= 1900 m and volume V= $1.6\pi c^2$ m^3. V represents the volume of the inflated nose of the propagating fracture, which is around a 10th of the estimated erupted volume (0.018 km^3)[2]. We set the rock properties to: ρ_r= 2900 kg·m^{-3}, μ=2·10^9 Pa and ν = 0.35 corresponding to the rock density, shear modulus and Poisson's ratio, respectively.

3 Effects defining the sills path

Stress intensity around the edge of a penny-shaped crack of volume V in a full-space, subject to a constant pressure, is defined by[12]:

$$K_I = \frac{3\mu V}{4(1-\nu)c^2\sqrt{\pi c}} \tag{1}$$

K_I around a crack under a pressure gradient is defined by[12]:

$$K_{I\alpha} = \frac{4}{3\pi}\Delta\gamma c\sqrt{\pi c}\cos(\alpha) \tag{2}$$

where α is the angle away from the direction of the linear stress gradient ($\Delta\gamma$) on the crack's walls. The pressure gradient in equation (2) defines the direction of K_{max} (blue lines in Fig. 2a). As such, ignoring other effects, the direction and sizes of competing pressure gradients acting on the crack define its propagation direction.

We now estimate stress gradients at Sierra Negra. First, we use an analytical solution describing stresses beneath a ridge-like topography[13]. h and v are the horizontal and vertical axis, respectively. We compute the horizontal gradient of vertical stress: $\delta\sigma_v/\delta h$, i.e. the normal stress gradient driving a flat-lying crack away from the caldera rim, at the inferred sill depth along its track. Linear stress gradients due to the difference of rock vs fluid density (buoyancy gradient) are[14]:

$$(\rho_r - \rho_f)g\sin(\beta) \tag{3}$$

where ρ_f is the magma density. The factor $\sin(\beta)$ means that if the crack is flat this gradient is zero. We set[15] $\rho_f = \rho_r - 300$ kg·m^{-3}. For the parameters above, 15 km from the caldera center (around where the sill began to turn) the dip needs to be around 10° for the buoyancy gradient to exceed the stress gradient due to the overlying slope (Extended Data Fig. 4) and drive the sill to turn away from the downslope direction (Fig. 2a).

As shown in Extended Data Fig. 5, a dipping sill is attracted towards the free surface. For c/d=2, as observed, a dip of 15° results in the same K_I increase for both buoyancy and free surface, doubling dips effects.

Lastly, we test if the other intrusions to the east that fed fissures 2, 3 and 4 (Fig. 1) may have attracted the sill. Two penny-shaped cracks subject to equal internal pressure[12,16] separated 5 km from each other, as observed (tip separation of 1.2 km) experience a maximal K_I increase of $\sim 3\%$. Such an increase is minor compared to the processes described earlier.

To summarise the analytical analysis, the stress gradient due to topography drives the sill away from the caldera rim. As the slope shallows, the buoyancy gradient begins to dominate even for shallowly dipping cracks, causing the sill to turn. The free surface amplifies this effect, Extended Data Fig. 7.

This analytical method of assessing the sill path is flexible and fast. In spite of its simplicity it can explain the trajectory of previous intrusions, including curved dyke trajectories such as the 2014 Bárðarbunga dyke path (Supplementary Information).

In order to allow interaction between all factors discussed above, we develop a 3D Boundary Element Model[9,10] to simulate a penny-shaped crack beneath the real edifice's topography. We include stresses due to gravitational loading and traction-free boundary conditions on the surface[9,17]. Using orientations of the crack in the 3D space obtained by inverting surface deformation (see Methods), our model explains the turning of the sill for snapshots along its path (Fig. 2), showing that it is the interaction between sill dip, slope gradients and the free surface that cause the observed turning. Note that increasing the ratio of the horizontal to vertical stress (σ_h/σ_v) in the topographic loading model results in better fits.

4 Full 3D propagation model

Lastly, we run full 3D fracture propagation simulations[10]. Here the crack is neither constrained to be planar nor circular in shape, only such that it maintains a constant V. The tip-line shape is recalculated at every iteration moving it forward in proportion to K/K_c, if $K/K_c >$ 1, at each triangle. We remove triangular elements that shut closed. Bending or twisting of the fracture's tip-line out of its plane is calculated using the maximum circumferential stress criterion[18].

In this last approach, we use a planar free-surface with a start height at $y = 0$ of 990 m with a slope of 3° facing to the north. The lithostatically stressed body ($\sigma_h = \sigma_v$) is loaded due to topography[13], Extended Data Fig. 4. We also apply throughout the body a compressive tectonic stress of 4.5 MPa directed along σ_{yy}, with σ_{xx} the mean between σ_{yy} and σ_{zz}, as suggested by stress indicators[19]. Shear stresses from the topographic loading solution[13] are set to zero, on the assumption that these stresses are diminished over time by faulting, diking and longer term rock deformation processes in the edifice's flanks.

The crack is started as an ellipse 1000 m wide and 5000 m long at a depth of 1000 m below sea level, dipping to the west by β=1°. K_c is set to 70 MPa·m$^{0.5}$. We find when the fracture gets a certain distance away from the caldera centre, it begins to turn and propagates east (Fig. 3). By changing the values of the parameters one at a time, we investigate the sensitivity of the path to the input parameters and initial geometry (Fig. 4). Reducing the initial start dip β or the buoyancy reduces the force driving the sill eastwards, causing the sill to stall as the topography shallows (Fig. 4, curves B to E). The start depth defines when the free-surface attraction takes effect (Extended Data Fig. 7F), such that only shallower sills can propagate eastwards (Fig. 4, curves F,G). The fracture toughness and volume define how far the sill can travel down-slope as the topography shallows. These also control the sill width, reducing the buoyancy force when this is smaller, again trapping the sill (Fig. 4, curves H to K). When the tectonic compressive stress is reduced, in places σ_v becomes the most compressive stress, causing the sills track to become very unstable with the sill quickly rising to the surface (Fig. 4L).

The simulations compare well with the observed trajectory; the sill was destined to turn, although it could have stalled or erupted earlier on its path.

5 Conclusions

Previous flank volcanism at Galápagos volcanoes has been fed by radial and circumferential dykes[4,20]. Here we have shown evidence of flank volcanism fed by a long curving sill. We find that trajectories of shallow sills underneath topography will be unstable and defined by a delicate balance between buoyancy forces, topographic load, external stresses and the free surface. Still, trajectories can be anticipated, provided all those factors are well-constrained and their interaction is accounted for. By combining such models with careful analysis of high-resolution crustal deformation data, we showed that such parameters as well as the state of stress of the volcano can be well constrained, reducing the uncertainties in the hazard.

Main references

1. Reynolds, R. W., Geist, D. & Kurz, M. D. Physical volcanology and structural development of Sierra Negra volcano, Isabela island, Galápagos archipelago. *Geological Society of America Bulletin* **107,** 1398–1410 (1995).
2. Vasconez, F. J. *et al.* The different characteristics of the recent eruptions of Fernandina and Sierra Negra volcanoes (Galápagos, Ecuador). *Volcanica* **1,** 127–133 (2018).
3. Sigmundsson, F. *et al.* Segmented lateral dyke growth in a rifting event at Bárðarbunga volcanic system, Iceland. *Nature* **517,** 191–195 (2015).
4. Bagnardi, M., Amelung, F. & Poland, M. P. A new model for the growth of basaltic shields based on deformation of Fernandina volcano, Galápagos Islands. *Earth and Planetary Science Letters* **377,** 358–366 (2013).
5. Smittarello, D. *et al.* Magma propagation at Piton de la Fournaise from joint inversion of InSAR and GNSS. *Journal of Geophysical Research: Solid Earth* **124,** 1361–1387 (2019).
6. Roman, A. & Jaupart, C. The impact of a volcanic edifice on intrusive and eruptive activity. *Earth and Planetary Science Letters* **408,** 1–8 (2014).
7. Rivalta, E. *et al.* Stress inversions to forecast magma pathways and eruptive vent location. *Science advances* **5,** eaau9784 (2019).
8. Dahm, T. Numerical simulations of the propagation path and the arrest of fluid-filled fractures in the Earth. *Geophysical Journal International* **141,** 623–638 (2000).
9. Davis, T., Healy, D. & Rivalta, E. Slip on wavy frictional faults: Is the 3rd dimension a sticking point? *Journal of Structural Geology* **119,** 33–49 (2019).
10. Davis, T., Rivalta, E. & Dahm, T. Critical fluid injection volumes for uncontrolled fracture ascent. *Geophysical Research Letters,* e2020GL087774 (2020).
11. Nikkhoo, M. & Walter, T. R. Triangular dislocation: an analytical, artefact-free solution. *Geophysical Journal International* **201,** 1119–1141 (2015).
12. Tada, H., Paris, P. & Irwin, G. *The Stress Analysis of Cracks Handbook; Third edition* 1 (New York: ASME Press, 2000).

13. Savage, W. Z., Powers, P. S. & Swolfs, H. S. *In situ geomechanics of crystalline and sedimentary rocks; Part V, RVT, a Fortran program for an exact elastic solution for tectonics and gravity stresses in isolated symmetric ridges and valleys* tech. rep. (US Geological Survey, Denver, Colorado, 1984).

14. Pollard, D. D. & Townsend, M. R. Fluid-filled fractures in Earth's lithosphere: Gravitational loading, interpenetration, and stable height of dikes and veins. *Journal of Structural Geology* **109,** 38–54 (2018).

15. Vigouroux, N. *et al.* 4D gravity changes associated with the 2005 eruption of Sierra Negra volcano, Galápagos. *Geophysics* **73,** WA29–WA35 (2008).

16. Fabrikant, V. Close interaction of coplanar circular cracks in an elastic medium. *Acta Mechanica* **67,** 39–59 (1987).

17. Martel, S. J. Modeling elastic stresses in long ridges with the displacement discontinuity method. *Pure and Applied Geophysics* **157,** 1039–1057 (2000).

18. Pollard, D., Pollard, D. D., Fletcher, R. C. & Fletcher, R. C. *Fundamentals of structural geology* (Cambridge University Press, 2005).

19. Heidbach, O. *et al.* The World Stress Map database release 2016: Crustal stress pattern across scales. *Tectonophysics* **744,** 484–498 (2018).

20. Chadwick Jr, W. & Dieterich, J. Mechanical modeling of circumferential and radial dike intrusion on Galapagos volcanoes. *Journal of Volcanology and Geothermal Research* **66,** 37–52 (1995).

21. Rosen, P., Gurrola, E., Agram, P. S., Sacco, G. F. & Lavalle, M. The InSAR Scientific Computing Environment (ISCE): A python framework for Earth science. *AGUFM* **2015,** IN11C–1789 (2015).

22. Wessel, B. *et al.* Accuracy assessment of the global TanDEM-X Digital Elevation Model with GPS data. *ISPRS Journal of Photogrammetry and Remote Sensing* **139,** 171–182 (2018).

23. Chen, C. W. & Zebker, H. A. Two-dimensional phase unwrapping with use of statistical models for cost functions in nonlinear optimization. *JOSA A* **18,** 338–351 (2001).

24. Bagnardi, M. & Hooper, A. Inversion of surface deformation data for rapid estimates of source parameters and uncertainties: A Bayesian approach. *Geochemistry, Geophysics, Geosystems* **19,** 2194–2211 (2018).

25. Decriem, J. *et al.* The 2008 May 29 earthquake doublet in SW Iceland. *Geophysical Journal International* **181,** 1128–1146 (2010).

26. Okada, Y. Surface deformation due to shear and tensile faults in a half-space. *Bulletin of the seismological society of America* **75,** 1135–1154 (1985).

27. Sun, R. J. Theoretical size of hydraulically induced horizontal fractures and corresponding surface uplift in an idealized medium. *Journal of Geophysical Research* **74,** 5995–6011 (1969).

Fig. 1. Interferogram spanning the sill propagation phase of the 2018 eruption. SAR data from the ALOS-2 satellite. Each colour cycle represents 11.45 cm of line-of-sight (LOS) surface displacement. Gray polygons show the extent of the lava flows emplaced during the time period spanned by the interferogram. Yellow lines mark the location and extent of all eruptive fissures. Black triangles mark the location of GPS stations. Black arrows show the satellite orbit direction (∼ N-S), look direction (∼ E-W), and the incidence angle in degrees. Descending pass, Track 147, ScanSAR mode.

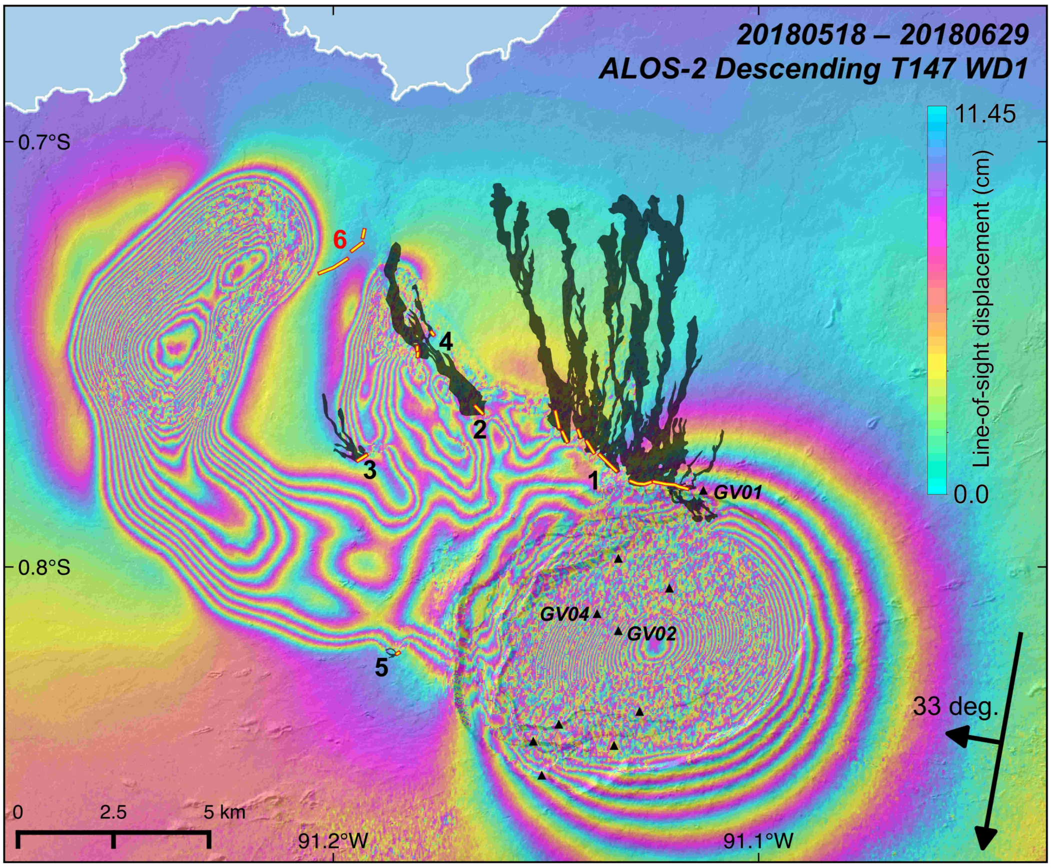

Fig. 2. Simulating the propagation direction of fracture at selected locations a) Analytical K_I diagram. Black circles represent the fracture, distance of the dashed gray line to the fracture edge represents K_I magnitude, blue segment represents K_{max} direction. Topographic contours in orange. b) Numerical simulation of the propagation direction at Sierra Negra. Fracture's scaled down to 1 km radius, white dashed-line represents K_I magnitude as in a). Dip and strike directions shown, defined by inversions (see Methods). For P7 a dip of 15° is used. Dashed grey outline is a contour of sill-induced deformation from Extended Data Fig. 3. Background σ_h/σ_v=0.5 in topographic loading model.

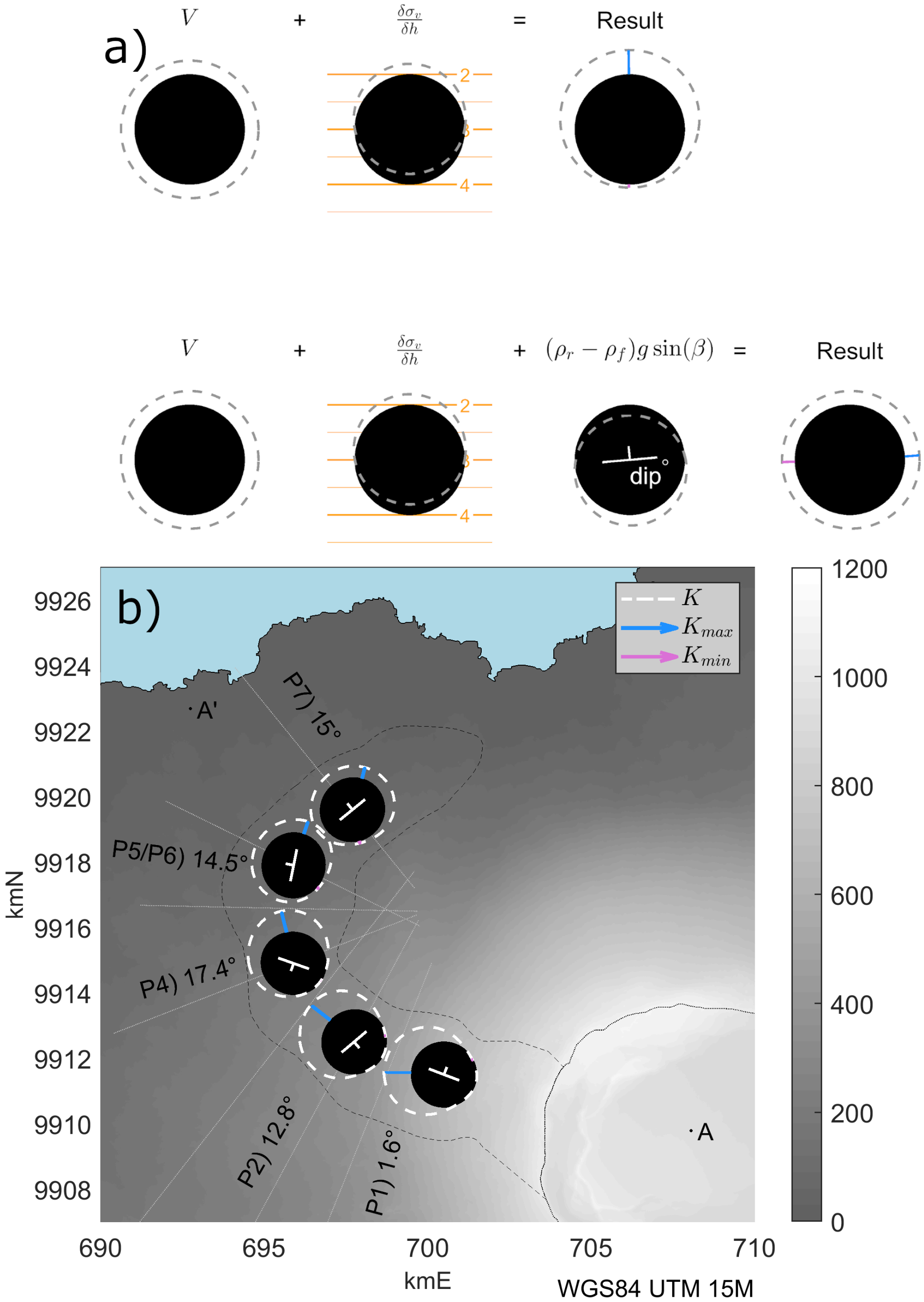

Fig. 3. Numerical simulation of the sill propagation. a) Map view, b) cross-section looking along the downslope direction and c) cross-section looking along the x-axis c). The fracture is shown at chosen locations along its computed path. Grey points are edges that closed in the previous iteration. The shaded patch in a) is the sill track and the dotted line the caldera rim. In c) the solid line is the topographic slope used to load the body and the dashed line is the simulations free-surface. Parameters used: $\beta = 1°$, $\rho_f = \rho_r - 300$ kg/m^3, start depth of 1000 m, $K_c = 70$ MPa$\cdot$ m$^{0.5}$, $V = \pi c^2 1.6$ m^3 and σ_{yy}=-4.5 MPa.

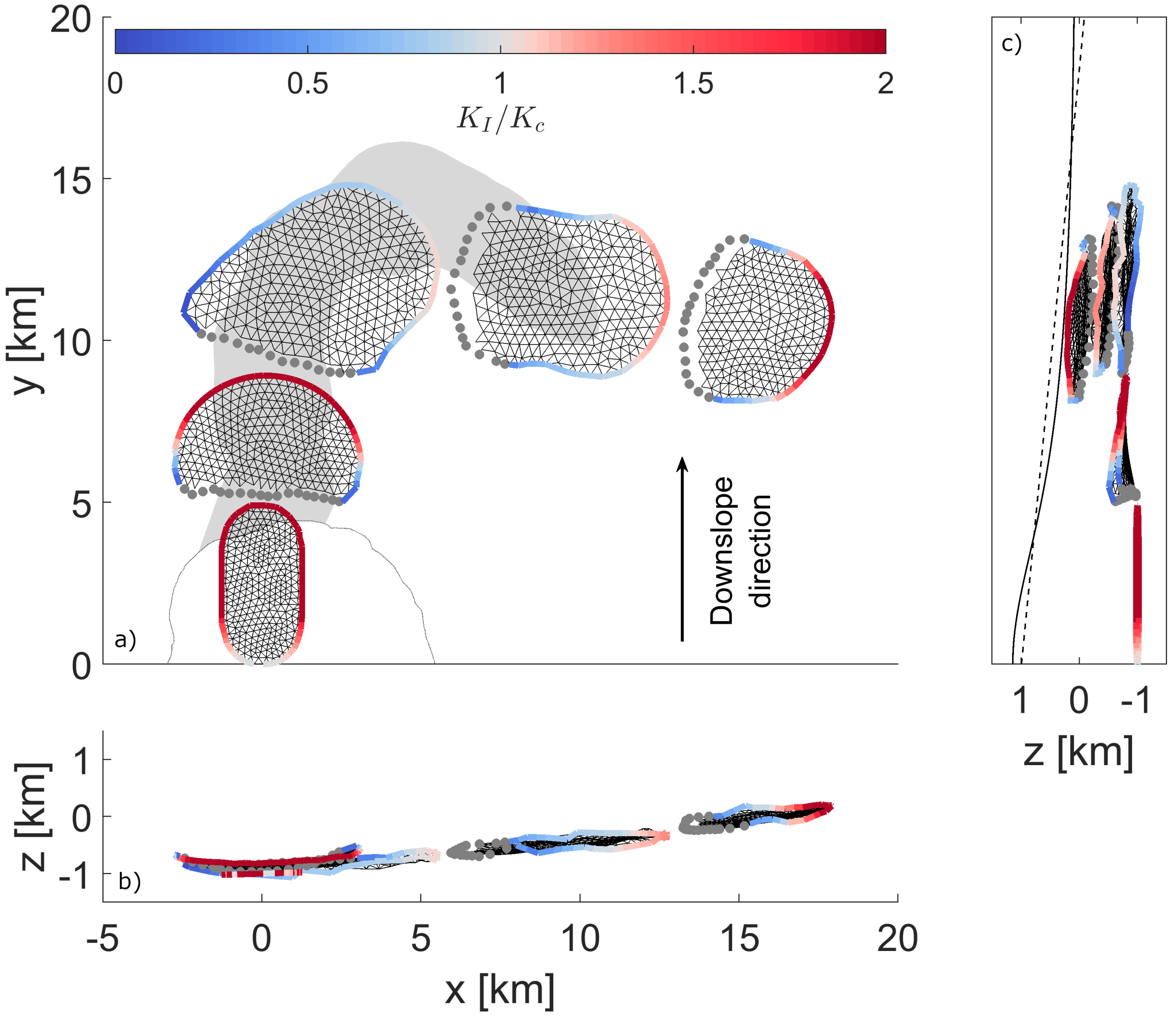

Fig. 4. Affects of parameters on the simulated sill path. Fracture paths from simulations as in Fig. 3, defined by the triangle with the maximum K value at each iteration. Dashed lines with blue dots are fractures that stalled, solid lines with red dots reached the free surface (erupted). In each simulation we changed one parameter with respect to Fig. 3, as follows: A is reference simulation from Fig. 3, B: $\beta = 1.5°$, C: $\beta = 0.5°$, D: $\rho_f = \rho_r - 450$ kg/m^3, E: $\rho_f = \rho_r - 150$ kg/m^3, F: Start depth=800 m, G: Start depth=1200 m, H: $K_c = 55$ MPa· m$^{0.5}$, I: $K_c = 85$ MPa· m$^{0.5}$, J: $V = \pi c^2 1.8$ m^3, K: $V = \pi c^2 1.4$ m^3 , L: σ_{yy}=-3 MPa, M: σ_{yy}=-6 MPa.

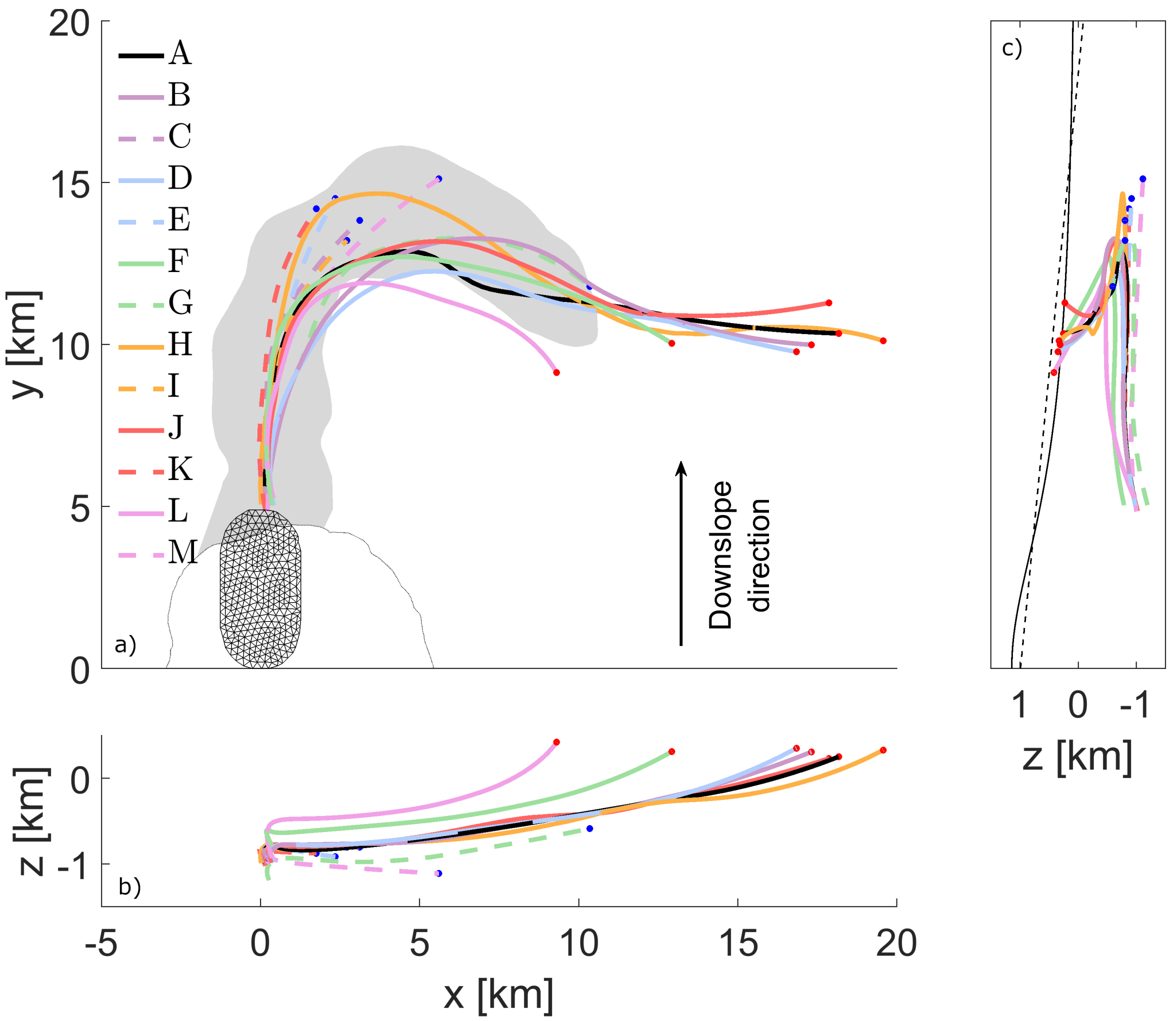

Methods

GPS data

Extended Data Fig. 1 shows the continuous GPS time series for three stations located at the summit of Sierra Negra (see Fig. 1 for station locations). Data downloaded from `http://geodesy.unr.edu`.

InSAR processing and additional observations

All interferograms were created using the InSAR Scientific Computing Environment (ISCE) software[21] and by applying conventional differential InSAR processing techniques for stripmap, ScanSAR (ALOS-2), and Terrain Observation by Progressive Scans (TOPS) (Sentinel-1) data. Topographic contributions to the interferometric phase are removed using the Deutsches Zentrum für Luft und Raumfahrt (DLR) 12-m resolution digital elevation model based on TanDEM-X satellite measurements[22], and interferograms are phase-unwrapped using the Statistical-cost, Network-flow Algorithm for Phase Unwrapping (SNAPHU)[23] implemented in ISCE.

InSAR inversions along track

Deformation source parameters and uncertainties are estimated using a Bayesian approach implemented in the Geodetic Bayesian Inversion Software[24]. The inversion algorithm samples posterior probability density functions (PDFs) of source parameters using a Markov chain Monte Carlo method, incorporating the Metropolis-Hastings algorithm, with automatic step size selection. Posterior PDFs are calculated considering errors in the InSAR data, which we directly quantify using experimental semivariograms to which we fit an unbounded exponential one-dimensional function with a nugget[24]. The exponential function is then used to populate the data variance-covariance matrix. Prior to inversions, all InSAR data sets are subsampled using an adaptive quadtree sampling[25] to reduce the computational burden when calculating the inverse of the data variance-covariance matrix and in forward model calculations. For all models, we assume that the deformation sources are embedded in an isotropic elastic half space with Poisson's ratio $\nu = 0.25$. Since no detailed prior information on the deformation source parameters are available, prior probability distributions are assumed to be uniform between geologically realistic bounds. In each inversion, posterior PDFs are sampled through 10^6 iterations. Depth estimates are referred to as distance from the surface.

At profile locations P1, P4 and P5 in Extended Data Fig. 6 we estimate source parameters of a rectangular dislocation with constant opening[26] and retrieve openings of 0.74±0.03 m, 1.73±0.03 and 2.80±0.03 respectively, where the value after ± brackets the 2.5 and 97.5 percentile of the results from our Bayesian inversion scheme[24], Extended Data Table. 1. Using such solutions the depth of this sill along its path is consistently 900-1000 m below the ground surface with a half-width of approximately 1.5 km.

Choosing physical parameters

We approximate the sill in our analytical analysis as a penny shaped crack. To retrieve c and V for this geometry, we compare the ground deformation of a flat lying rectangular dislocation where the faces open 2 m with a depth d of 950 m and its third axis extending far out of the plane of observation, to the the analytical solution describing the uplift due a pressurised penny-shaped crack under a half space with the same d[27]. The penny-shaped cracks ground deformation supplies a radial deformation pattern, therefore we only fit this to the ground deformation relative to the short-axis of the sill. Once fitted, we retrieve a radius c= 1900 m and volume V of = $\pi c^2 1.6$ (with the largest error 1.5% and 15% less than the maximum u_z and u_x value from the dislocation solution, respectively).

Comparison of different effects on stress intensity factors

Extended Data Fig. 5 is computed using a numerical scheme to evaluate how K_I (equation (1)) decreases as the crack approaches the half-space surface[9]. For c/d=2 as observed, a dip of 15° causes a relative increase and decrease of K_I of +30% -10% at its highest and lowest edge respectively. A 30% increase corresponds to the same K_I increase as a sill dip of around 15° due to $(\rho_r - \rho_f)g\sin(\beta)$. As with buoyancy, this effect increases with crack dip.

End notes

Data availability statement

Computed interferograms that support the findings of this study are achieved as geoTIFF files on Zenodo at http://... Sentinel-1 raw SAR data that support the findings of this study are publicly available at https://scihub.copernicus.eu. ALOS-2 raw SAR data availability is restricted to PI investigation at www.eorc.jaxa.jp/ALOS/en/.

Code availability statement

The code used for boundary element numerical analysis in this study was the open source code `https://doi.org/10.5281/zenodo.3694163` with an interface with the Computational Geometry Algorithms Library software (C++) for meshing.

Acknowledgements

T Davis is funded by the DFG-ICDP grant N. RI 2782/3-1. M. Bagnardi was supported by an appointment to the NASA Postdoctoral Program at the Jet Propulsion Laboratory, administered by the Universities Space Research Association (USRA) through a contract with NASA. Part of this research was carried out at the Jet Propulsion Laboratory, California Institute of Technology, under a contract with the National Aeronautics and Space Administration (grant 281945.02.47.04.51).

Author Contributions

T.D and M.B coordinated the work and wrote the initial manuscript. M.B and P.L acquired and analysed the InSAR and GPS data in this study. This analysis provided the evolution and geometry of the sill. T.D and E.R conceptualised the analytical and numerical fracture mechanics that form the interpretation in this work. T.D wrote the analytical and numerical fracture mechanics codes used in this study. All authors have read and revised the manuscript and contributed ideas to the research.

Additional Information

Supplementary Information is available for this paper. Correspondence and requests for materials should be addressed to T.Davis.

Methods references

9. Davis, T., Healy, D. & Rivalta, E. Slip on wavy frictional faults: Is the 3rd dimension a sticking point? *Journal of Structural Geology* **119,** 33–49 (2019).

21. Rosen, P., Gurrola, E., Agram, P. S., Sacco, G. F. & Lavalle, M. The InSAR Scientific Computing Environment (ISCE): A python framework for Earth science. *AGUFM* **2015,** IN11C–1789 (2015).

22. Wessel, B. *et al.* Accuracy assessment of the global TanDEM-X Digital Elevation Model with GPS data. *ISPRS Journal of Photogrammetry and Remote Sensing* **139,** 171–182 (2018).

23. Chen, C. W. & Zebker, H. A. Two-dimensional phase unwrapping with use of statistical models for cost functions in nonlinear optimization. *JOSA A* **18,** 338–351 (2001).

24. Bagnardi, M. & Hooper, A. Inversion of surface deformation data for rapid estimates of source parameters and uncertainties: A Bayesian approach. *Geochemistry, Geophysics, Geosystems* **19,** 2194–2211 (2018).

25. Decriem, J. *et al.* The 2008 May 29 earthquake doublet in SW Iceland. *Geophysical Journal International* **181,** 1128–1146 (2010).

26. Okada, Y. Surface deformation due to shear and tensile faults in a half-space. *Bulletin of the seismological society of America* **75,** 1135–1154 (1985).

27. Sun, R. J. Theoretical size of hydraulically induced horizontal fractures and corresponding surface uplift in an idealized medium. *Journal of Geophysical Research* **74,** 5995–6011 (1969).

325 ## Extended Data

Extended Data Table. 1. Bayesian inversion results for profiles shown in Extended Data Fig. 6, using rectangular dislocations[26]. The 2.5 percentile value, the maximum a posteriori probability solution, and the 97.5 percentile value are shown for each parameter. The results for P7 are not shown, due to unsatisfactory fits to the data.

Profile	Opening [m]	Dip°	Dip Direction°	Depth [m]	Down-dip width [m]	Along-strike width [m]
P1	0.7 / 0.7 / 0.8	0.6 / 1.6 / 2.7	19 / 21 / 23	861 / 899 / 958	2907 / 2949 / 2986	2554 / 3175 / 4503
P2	1.0 / 1.0 / 1.0	11.0 / 12.8 / 15.4	136 / 140 / 142	998 / 1058 / 1335	2527 / 2637 / 3787	2356 / 2387 / 2421
P3	1.2 / 1.2 / 1.2	3.0 / 5.5 / 7.5	138 / 140 / 142	939 / 992 / 1040	3541 / 3891 / 13903	2119 / 2140 / 2172
P4	1.7 / 1.8 / 1.8	16.7 / 17.4 / 18.1	199 / 199 / 200	1053 / 1084 / 1115	3296 / 3604 / 3653	1754 / 1771 / 1789
P5	2.8 / 2.8 / 2.8	14.0 / 14.5 / 15.0	210 / 210 / 210	994 / 1010 / 1026	2196 / 2210 / 2224	2838 / 2850 / 2859
P6	2.80 / 2.83 / 2.85	14.1 / 14.6 / 14.9	352 / 353 / 353	976 / 993 / 1007	2322 / 2340 / 2353	2826 / 2840 / 2851

Extended Data Fig. 1. Vertical GPS movement's from continuous GPS stations GV01, 02 and 04 situated on Sierra Negra's summit. See Fig. 1 for station location.

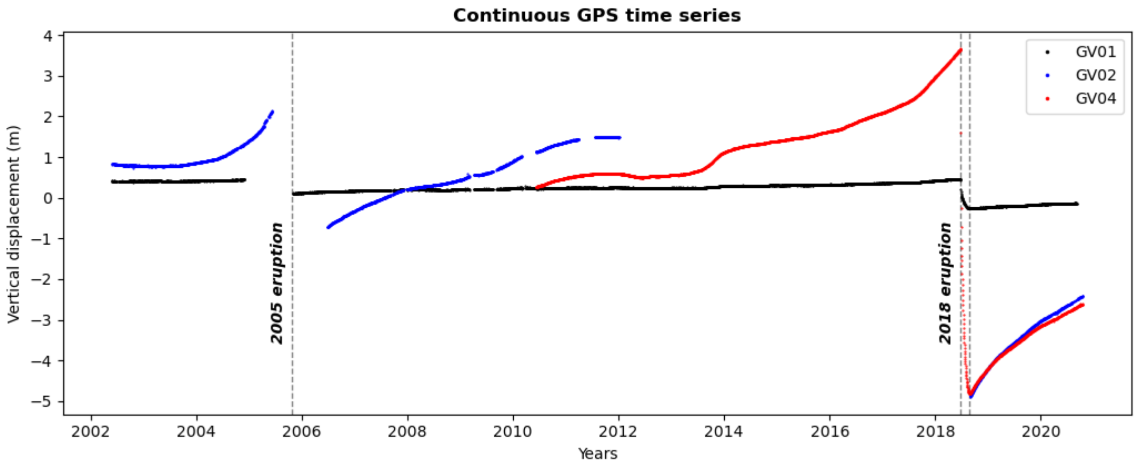

Extended Data Fig. 2. Interferograms of Sierra Negra spanning the sill propagation phase of the 2018 eruption. SAR data are from the Sentinel-1 satellite. Same colourbar as Fig. 1, with each colour cycle as 2.8 cm of LOS ground displacement. Black arrows show the satellite orbit direction, a) ∼ S-N b) ∼ N-S, look direction a) ∼ W-E b) ∼ E-W, and the incidence angle in degrees. a) Ascending pass, Track 61 TOPS mode. b) Descending pass, Track 106, TOPS mode. Symbols as in Fig. 1 in the main text.

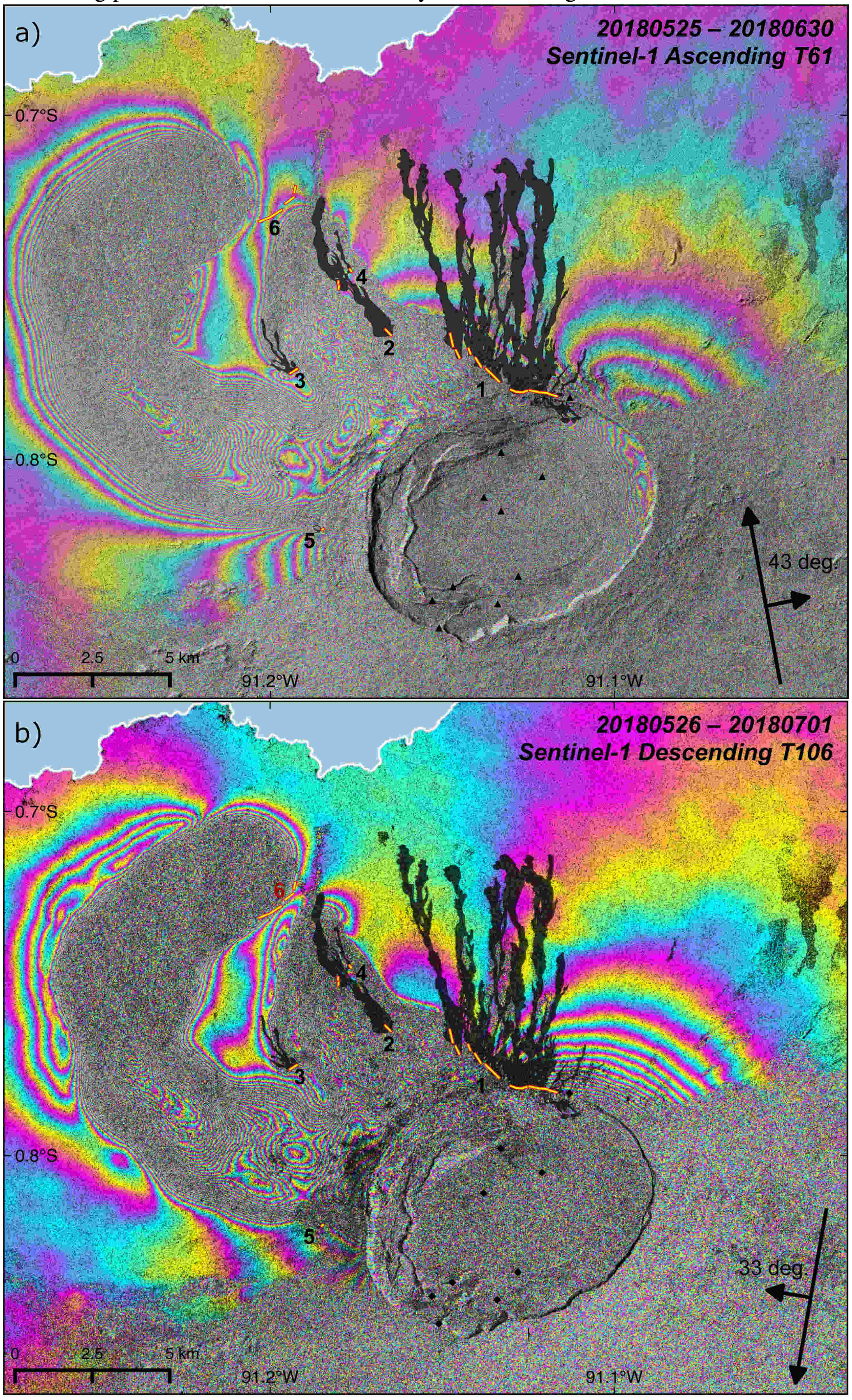

Extended Data Fig. 3. Interferograms of Sierra Negra spanning the whole propagation and early eruption phase of the 2018 eruption. SAR data are from the ALOS-2 satellite. Colourbar as Fig. 1, with each colour cycle as 11.45 cm LOS ground displacement. Black arrows show the satellite orbit direction, a) ∼ S-N b) ∼ N-S, look direction a) ∼ W-E b) ∼ E-W, and the incidence angle in degrees. a) Ascending pass, Track 41, Fine Stripmap mode (SM3; pixel resolution 9.1x5.3 m). b) Descending pass, Track 147, Ultra-fine Stripmap mode (SM1; pixel resolution 3.0x3.0 m). Symbols as in Fig. 1 in the main text.

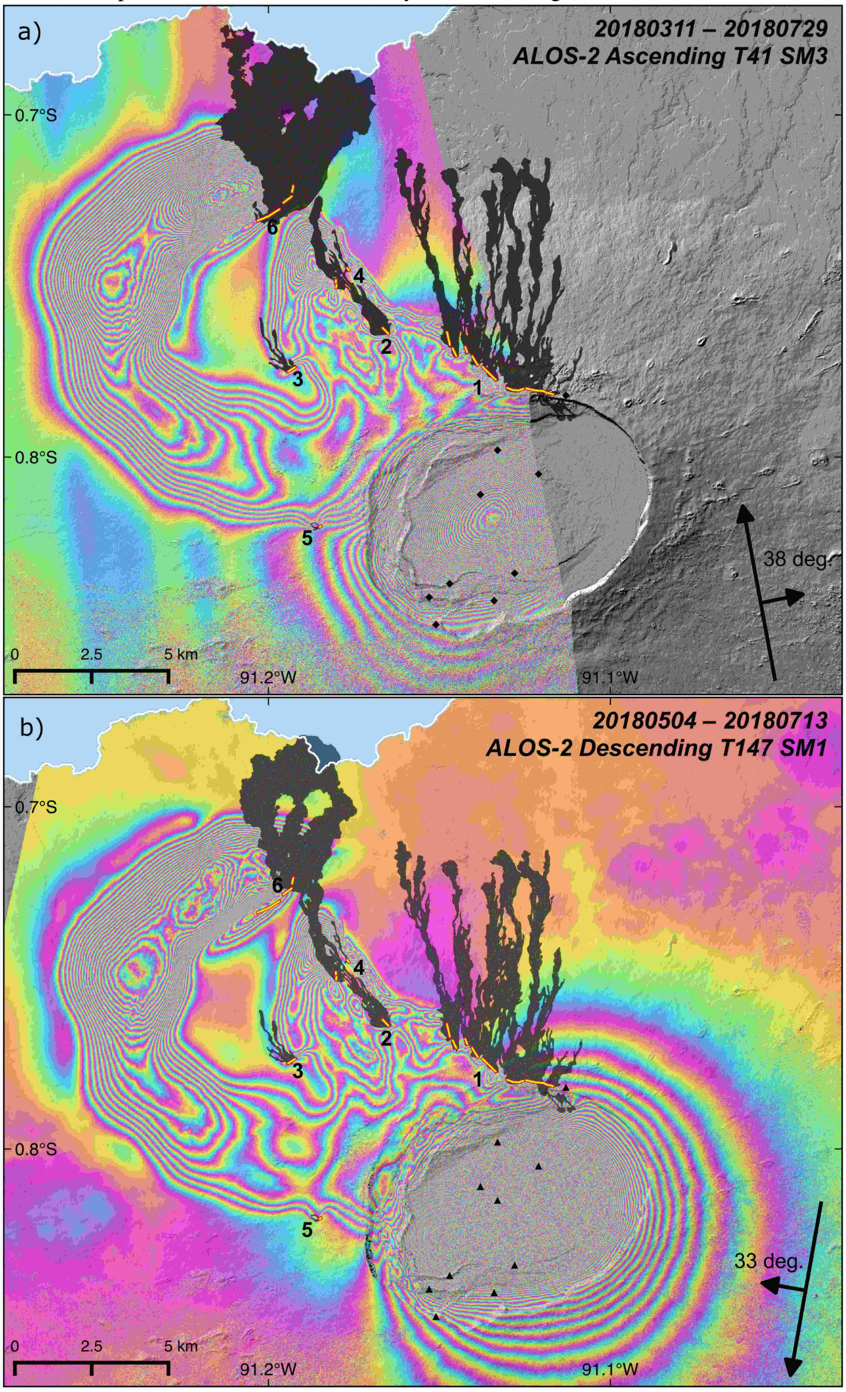

Extended Data Fig. 4. **Magnitude of stress gradients, topographic vs buoyancy.** Top panel shows the topographic profile of the volcano and an approximation of this profile using[13]. Bottom panel shows the required crack dip β such that the two competing gradients match, according to $(\rho_r - \rho_f)g\sin(\beta) = \delta\sigma_v/\delta h$. The numerical result from the profile A-A' shown in Fig. 2 is shown in black, the analytical result is shown in blue.

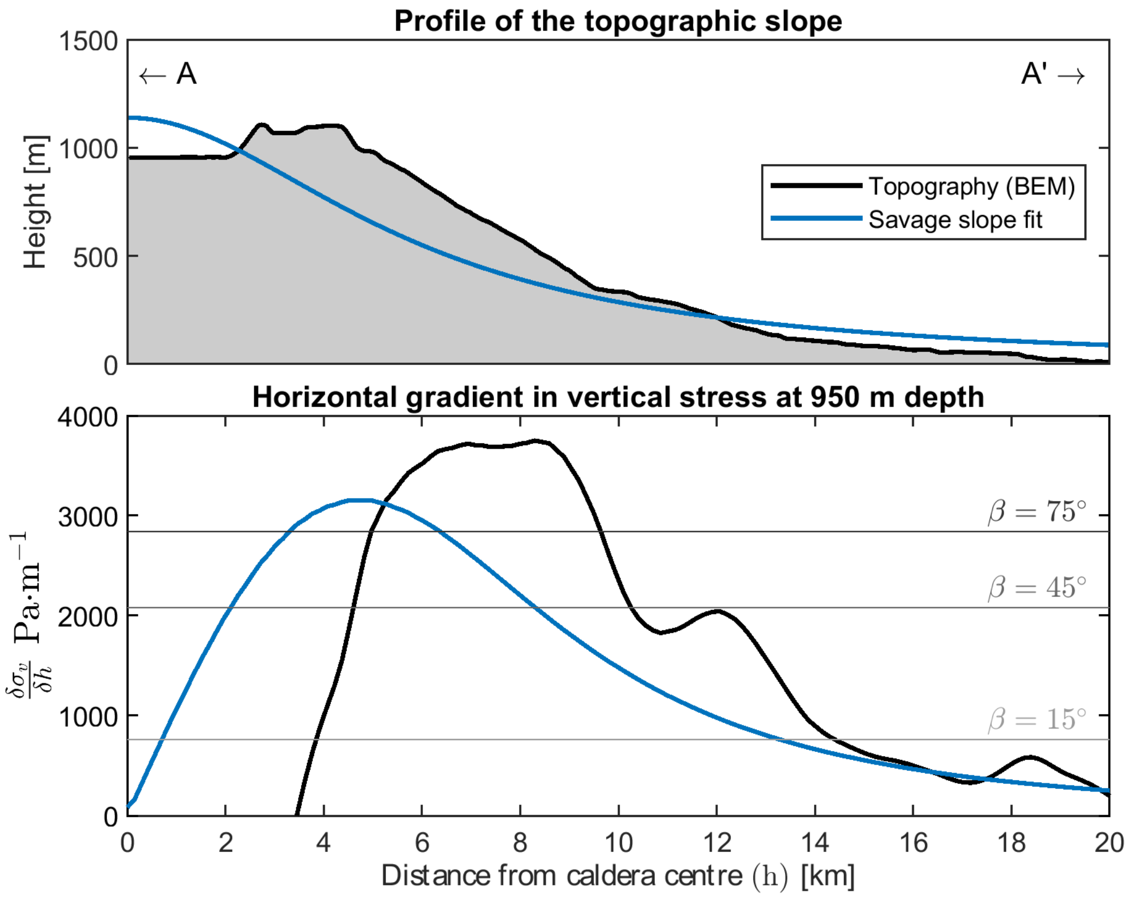

Extended Data Fig. 5. Half-space effects on K_I at the upper and lower tips of a dipping penny-shaped crack. Maximum and minimum K_I values (solid and dashed) for constant volume cracks, depth d below a half-space, with radius c. Values relative to K_∞, equation (1)). Note the offset from 1 when c/d=0, indicates the size of the numerical error.

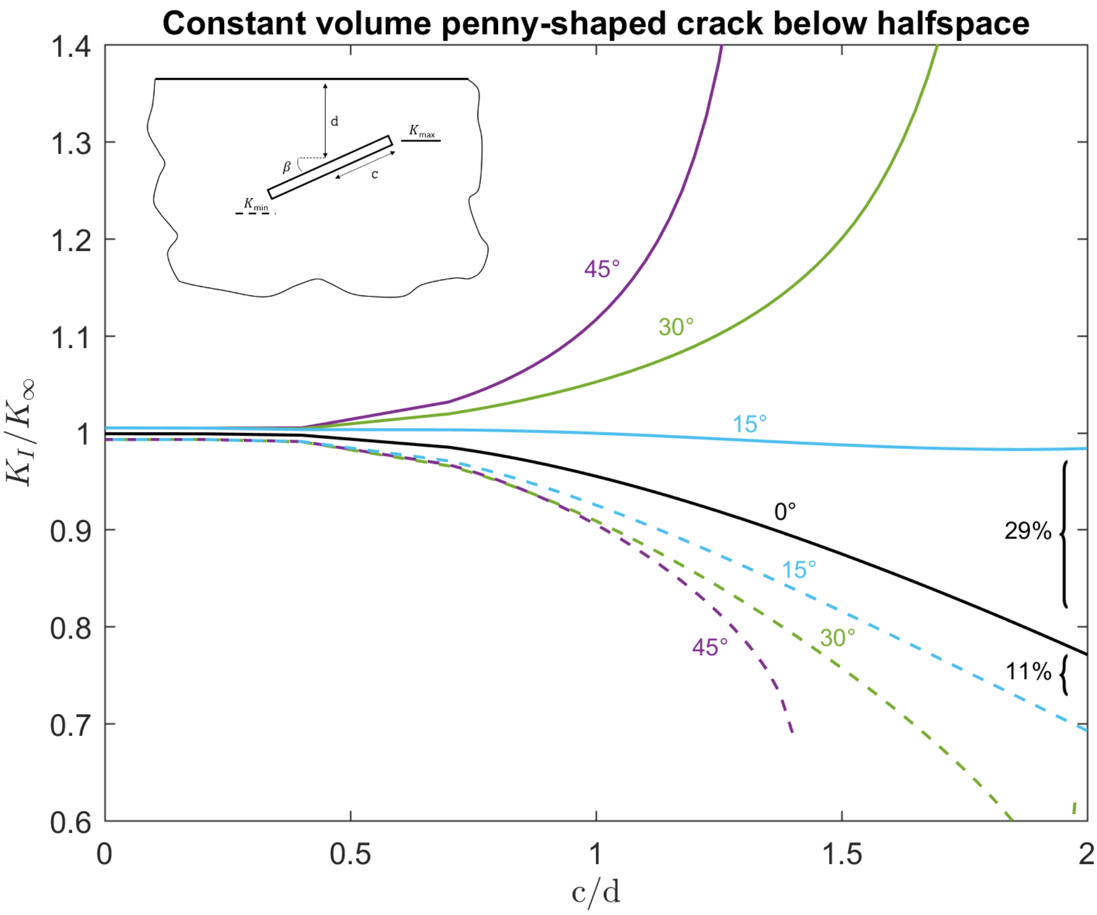

Extended Data Fig. 6. Profiles used to estimate intrusion geometry. a) InSAE as Extended Data Fig. 3 with the location of the profiles (P1 - P7) marked by blue shading. Gray polygons show the extent of the lava flows emplaced during the time period spanned by the interferogram. Yellow lines mark the location and extent of all eruptive fissures. b) Each plot shows the line-of-sight ground displacement for each data point included in profiles 1-7. Vertical scale is not constant. c) All profiles shown on one plot, (∼ W-E).

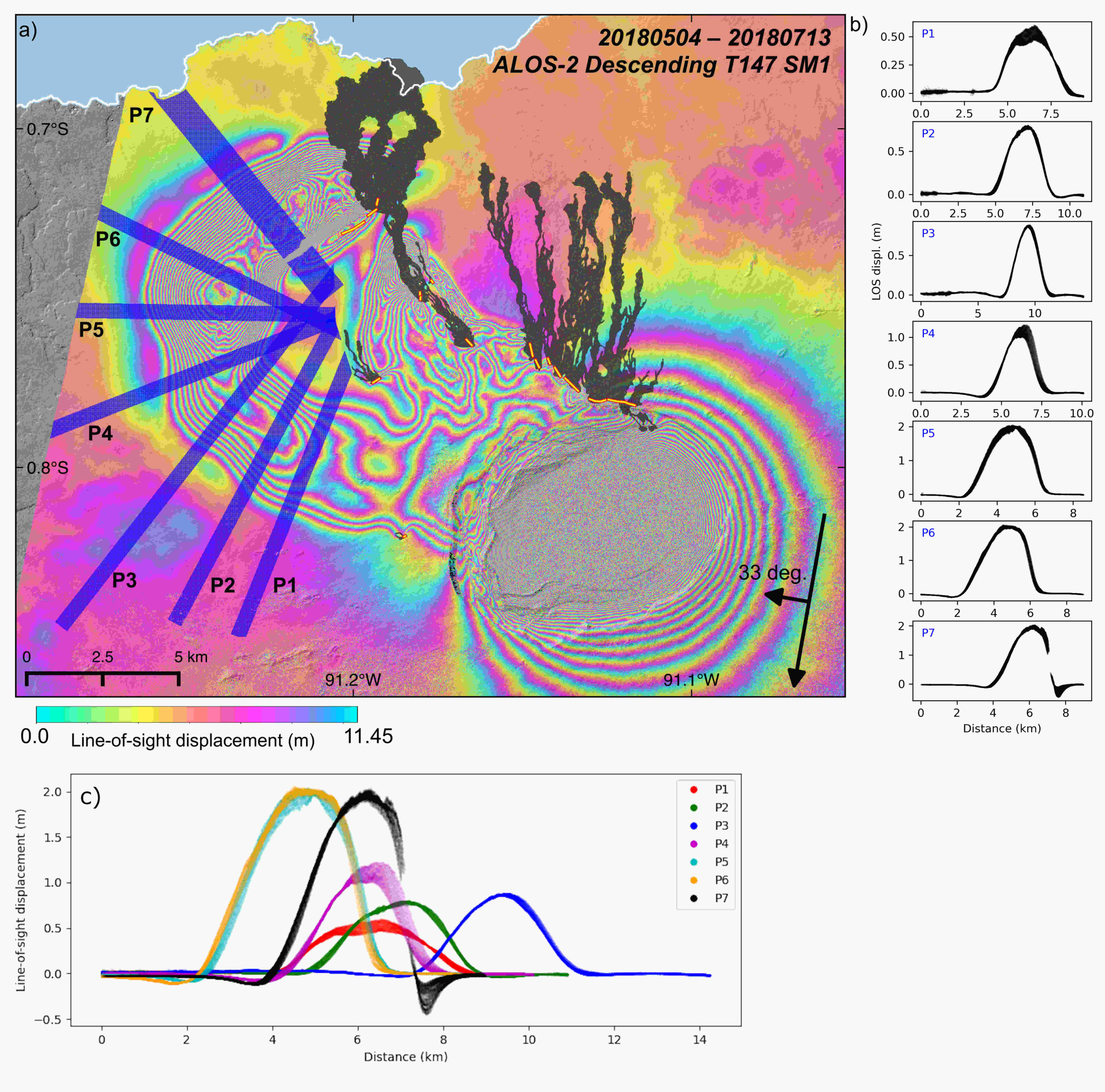

Extended Data Fig. 7. Summary of changes in K due to different effects on the sill at Sierra Negra.

Cross sections of cracks showing changes in stress intensity, K_I, at the crack tip due to different processes. Crack opening exaggerated by 300, red patches show the 2nd invariant of stress computed from K at the tip. a) crack in a full space, b) crack under topographic stress gradient, topography exaggerated, c) crack with 15° dip, buoyancy as defined in text, d) interacting cracks with separation defined in text, e) flat crack close to the half space, f) crack close to half space with dip, only internal pressure.

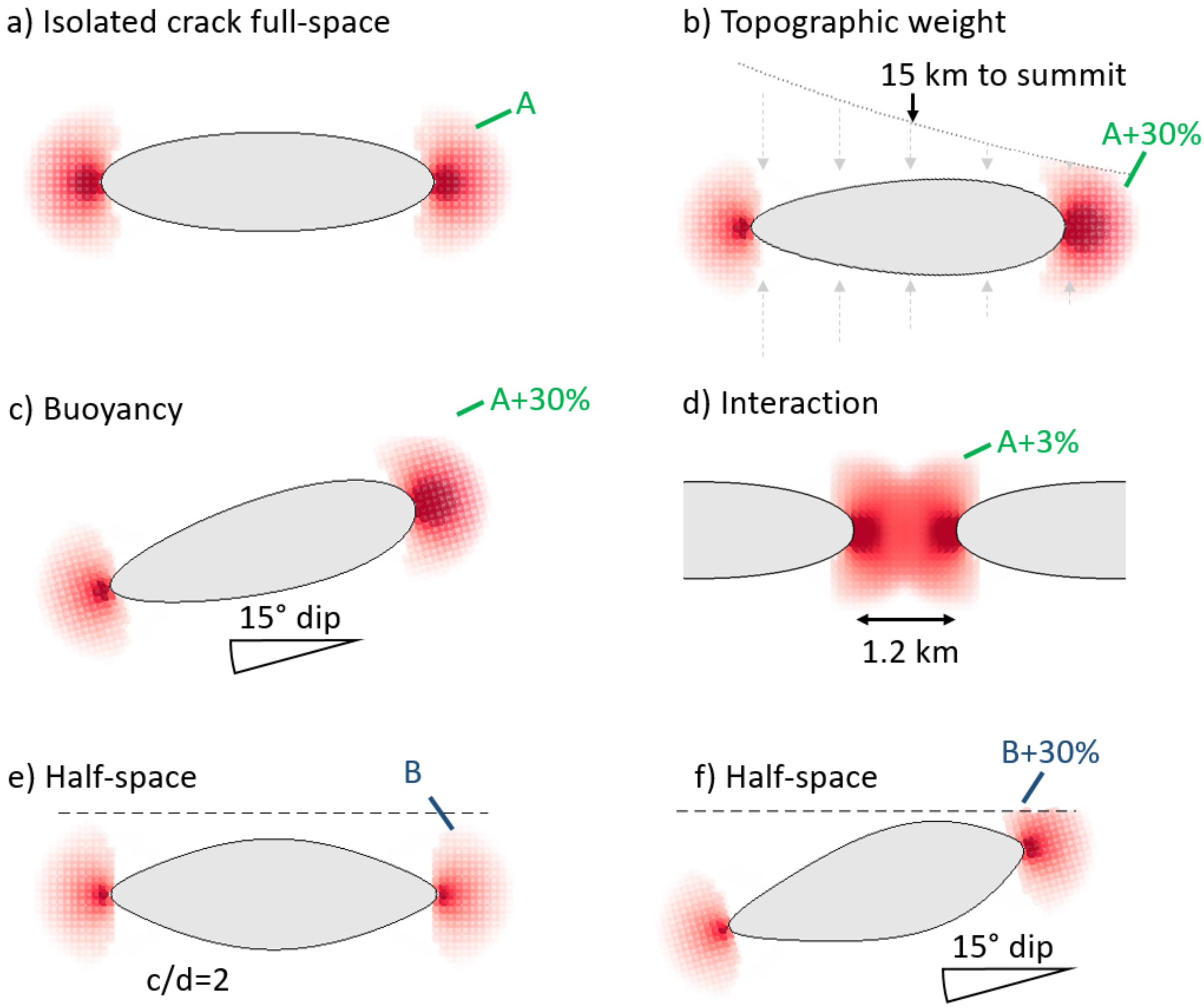

Extended Data Fig. 8. Comparison of K_I around a penny-shaped and elongated penny-shaped crack.

a) The mesh used for this analysis. θ is defined in degrees away from the tip ($y = 1$). Comparison of K_I from equation (2 to that for an elongated penny-shaped crack as in a), assuming b) a stress gradient along the x-axis; c) a stress gradient along the y-axis. d) Comparison of K_I from equation (1) to that for an elongated penny-shaped crack with uniform pressure. Note some slight numerical inaccuracies are present.

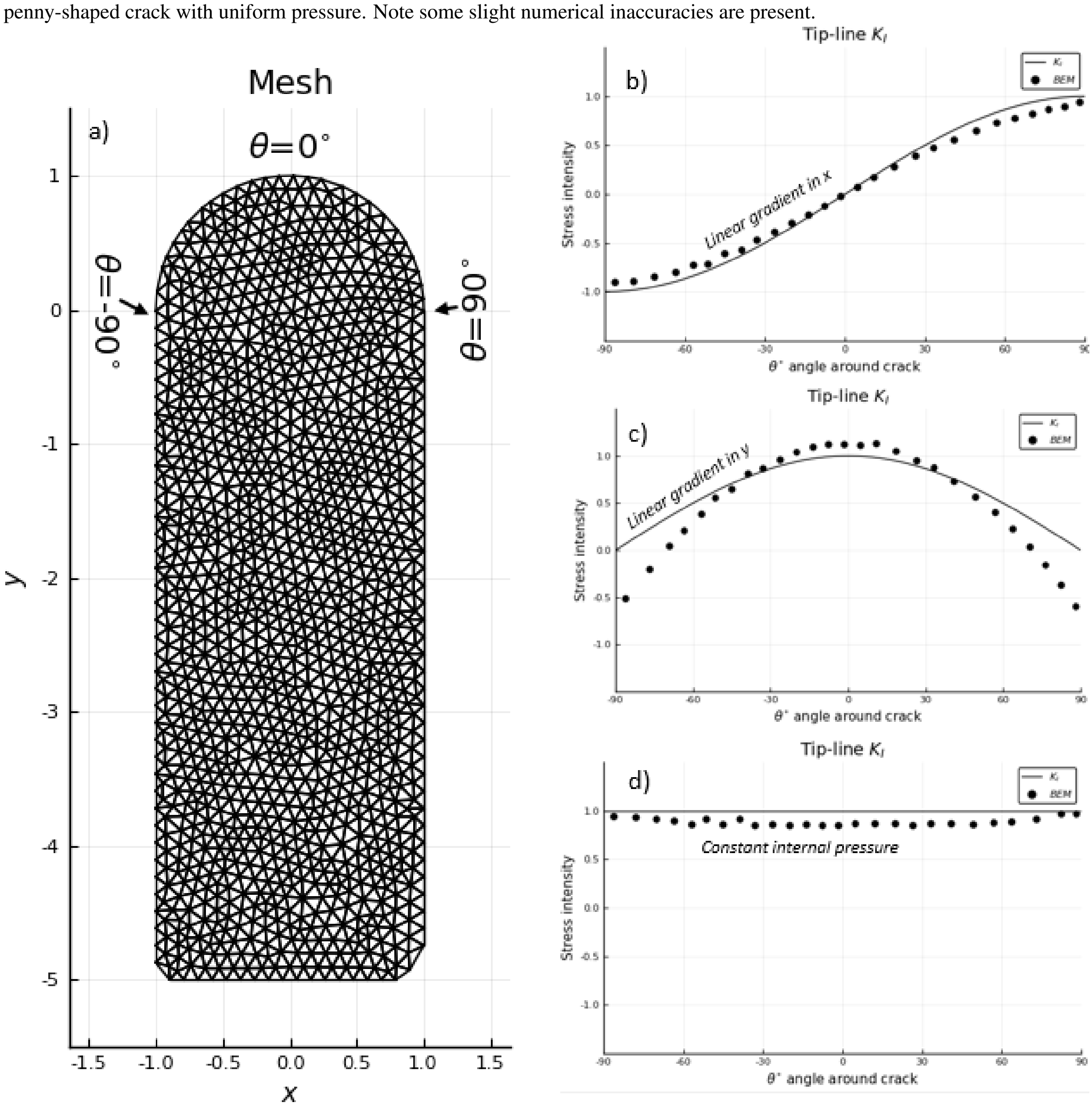

Extended Data Fig. 9. Forecasting propagation directions along the Bárðarbunga dyke track. Numbered labels indicate the position of the penny at test locations as in[3]. Preferred directions of propagation, according to equation (SI.2), where the maximum circumferential (hoop) stress is shown in blue.

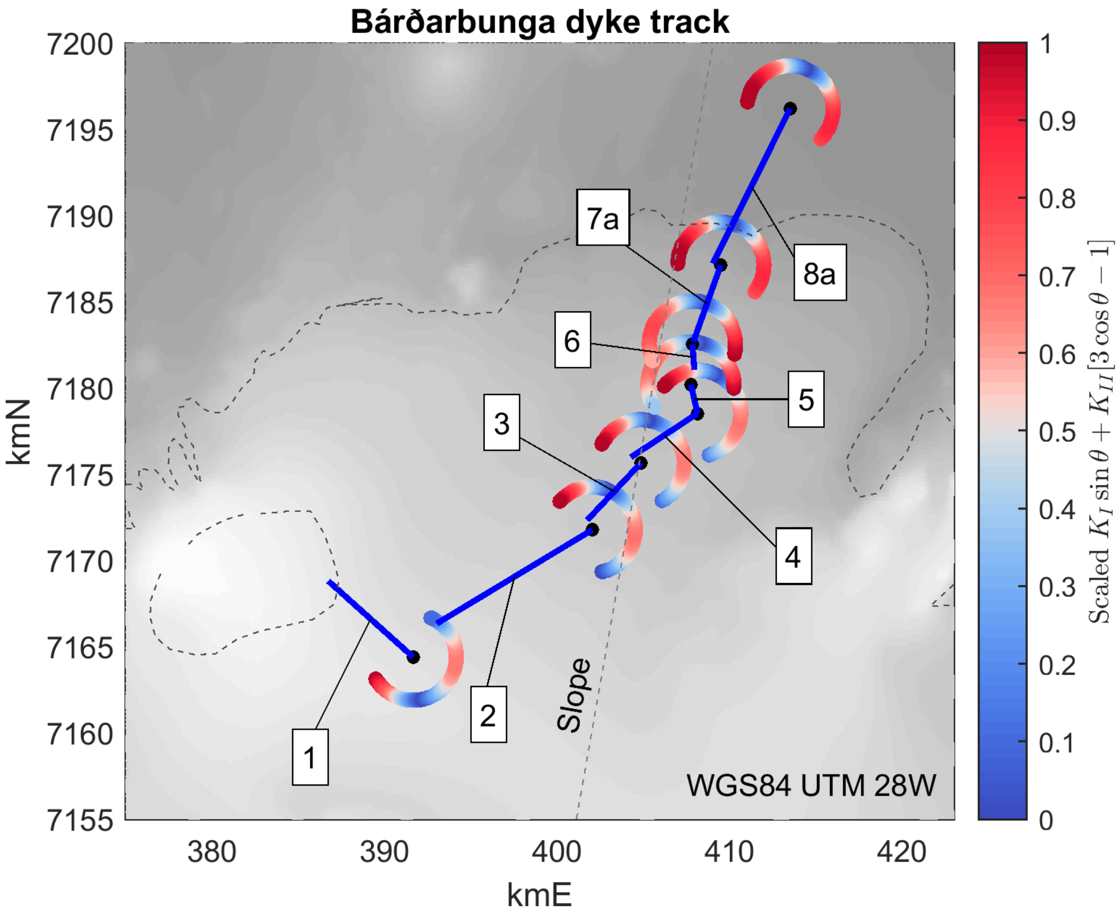

Supplementary Information

Approximating sill geometry as a penny

Here we estimate the error associated with approximating a 3D propagating crack as penny-shaped. We compare analytical formulas that describe K around the tip-line of penny-shaped cracks under uniform pressure (equation (1)) and linear stress gradients (equation (2)) to those of a more realistic 3D shape as in Extended Data Fig. 8a. We apply stresses and pressures so that at the point of maximum opening of the penny's crack walls, the opening of lengthened-tail crack walls is equal. This location for penny-shaped cracks with constant internal pressure is the crack centre (0,0), whereas for a linear gradient it is located along the direction of the stress gradient ($\sin(\pi/4)c$). We find the analytical formulas capture the scale and shape of the problem with some deviations (Extended Data Fig. 8b, c and d. Note the accuracy of the numerical boundary element method to approximate K is described in[9,10] and the mesh used in Extended Data Fig. 8 has $\sim$2000 triangles.

Reproducing Bárðarbunga's track

Here we test our analytical approach of approximating the crack as a series of isolated pennies on the case of the Bárðarbunga 2018 dyke track. The aim is to test how well the assumptions of our method perform in comparison to methods that take into account the entire dyke surface[3].

We use a series of vertical pennies with c=2000 m, d=4000 m, V=$\pi c^2$3 m^3 (i.e. opening of 3 m if constant), ν=0.25, μ=2E$\cdot$10^9 pa, . All stresses are evaluated at the crack centre. Following[3], we define the tectonic stress as that due to a vertical semi-infinite buried dislocation of 4 m opening with an upper tip depth of 10 km, centred at Askja volcano and striking at 12°. As before, we use an analytical solution describing stresses beneath topographic slopes using a state of perfect confinement[13], applied along the straight dashed line shown in Extended Data Fig. 9. K_I around the tip-line is defined by the internal volume through equation (1), and by the gradient in normal traction taken from the slope stress solution, Eq.2. Shear stresses due to the tectonic and gravitational stress are resolved as shear traction (t_s) on the plane of the dyke and K_{II} is computed with:

$$K_{II} = \frac{4t_s\sqrt{c/\pi}}{2-\nu} \tag{SI.1}$$

We compute K at the leading tip of the penny (black dots in Extended Data Fig. 9). Half-space effects on values of K_I and K_{II} are below 10%, even with c/d ratios of 0.99. Turning of the leading tip is then computed using:

$$K_I \sin\theta + K_{II}[3\cos\theta - 1] \tag{SI.2}$$

where the minimum value corresponds to the direction of the greatest circumferential stress (θ_0=0) close to the tip, and as such the potential propagation direction,[18]. We find our analytical approach predicts the dyke's pathway in a computationally efficient way Extended Data Fig. 9.

Supplementary material references

3. Sigmundsson, F. *et al.* Segmented lateral dyke growth in a rifting event at Bárðarbunga volcanic system, Iceland. *Nature* **517,** 191–195 (2015).
9. Davis, T., Healy, D. & Rivalta, E. Slip on wavy frictional faults: Is the 3rd dimension a sticking point? *Journal of Structural Geology* **119,** 33–49 (2019).
10. Davis, T., Rivalta, E. & Dahm, T. Critical fluid injection volumes for uncontrolled fracture ascent. *Geophysical Research Letters,* e2020GL087774 (2020).
13. Savage, W. Z., Powers, P. S. & Swolfs, H. S. *In situ geomechanics of crystalline and sedimentary rocks; Part V, RVT, a Fortran program for an exact elastic solution for tectonics and gravity stresses in isolated symmetric ridges and valleys* tech. rep. (US Geological Survey, Denver, Colorado, 1984).
18. Pollard, D., Pollard, D. D., Fletcher, R. C. & Fletcher, R. C. *Fundamentals of structural geology* (Cambridge University Press, 2005).